Available online at www.sciencedirect.com

ScienceDirect

Comput. Methods Appl. Mech. Engrg. 404 (2023) 115767

Computer methods in applied mechanics and engineering

www.elsevier.com/locate/cma

A novel hybrid IGA-EIEQ numerical method for the Allen–Cahn/Cahn–Hilliard equations on complex curved surfaces

Qing Pan[a], Chong Chen[b], Yongjie Jessica Zhang[c], Xiaofeng Yang[d],*

[a] *School of Computer and Communication Engineering, Changsha University of Science & Technology, Changsha, 410114, China*
[b] *LSEC, ICMSEC, Academy of Mathematics and Systems Science, Chinese Academy of Sciences, Beijing, 100190, China*
[c] *Department of Mechanical Engineering, Carnegie Mellon University, Pittsburgh, PA 15213, USA*
[d] *Department of Mathematics, University of South Carolina, Columbia, SC 29208, USA*

Received 30 August 2022; received in revised form 3 November 2022; accepted 6 November 2022
Available online xxxx

Abstract

We present an efficient fully discrete algorithm for solving the Allen–Cahn and Cahn–Hilliard equations on complex curved surfaces. The spatial discretization employs the recently developed IGA (isogeometric analysis) framework, where we adopt the strategy of Loop subdivision with the superior adaptability of any topological structure, and the basis functions are quartic box-splines used to define the subdivided surface. The time discretization is based on the so-called EIEQ (explicit-Invariant Energy Quadratization) approach, which applies multiple newly defined variables to linearize the nonlinear potential and realize the efficient decoupled type computation. The combination of these two methods can help us to gain a linear, second-order time accurate scheme with the property of unconditional energy stability, whose rigorous proof is given. We also develop a nonlocal splitting technique such that we only need to solve decoupled, constant-coefficient elliptic equations at each time step. Finally, the effectiveness of the developed numerical algorithm is verified by various numerical experiments on the complex benchmark curved surfaces such as bunny, splayed, and head surfaces.

Keywords: Loop subdivision; IGA-EIEQ; Decoupled; Unconditional energy stability; Allen–Cahn; Cahn–Hilliard

1. Introduction

As representative equations of the phase-field (diffusive interface) approach, the Allen–Cahn and Cahn–Hilliard equations, originally introduced by Allen and Cahn in [1] to describe the motion of the anti-phase boundaries in crystalline solids, and Cahn and Hilliard in [2] to simulate the complicated phase separation and coarsening phenomena in a solid, respectively, have been extensively studied and widely used in many complicated moving interface problems in various science and engineering fields, such as computational biology, materials science, and fluid dynamics. It is very challenging to develop accurate and efficient numerical schemes to solve these two equations. Noting that some special phase separation or fluid flow dynamics may appear on static and dynamic surfaces, such as phase separation on lipid bilayer membranes [3–5] and dendritic crystal growth on curved

* Corresponding author.
E-mail addresses: panqing@lsec.cc.ac.cn (Q. Pan), chench@lsec.cc.ac.cn (C. Chen), jessicaz@andrew.cmu.edu (Y.J. Zhang), xfyang@math.sc.edu (X. Yang).

https://doi.org/10.1016/j.cma.2022.115767
0045-7825/© 2022 Elsevier B.V. All rights reserved.

surfaces [6], therefore, numerical study of the interface dynamics of the Allen–Cahn and Cahn–Hilliard equations on complex curved surfaces is of great significance and practical applications.

For numerical analysis of partial differential equations (PDEs) on surfaces, there are many successful numerical algorithms such as finite difference method [7], spectral method [8,9] and finite element method (FEM) [10]. Although the first two methods have made significant progress in recent years, most of the problems they deal with are still limited to simple domains, e.g., rectangular, circular, or spherical regions. The latter one, FEM, can efficiently deal with various irregular surfaces in practical engineering, see [11–13] for theoretical/numerical studies of phase transition-related models on surfaces. However, it is remarkable that the FEM involves the approximation of surface differential geometric operators, which may introduce additional errors caused by numerical approximation schemes. We can see that the variation of the Laplacian operator on the surface requires integrating the derivative product of the surface itself. Traditional FEM requires costly and time-consuming human intervention, and encounters great difficulties in the refining process, especially for complex geometries. Therefore, for the spatial discretization of surfaces, this paper adopts the IGA method, see [14,15].

The IGA method uses the non-uniform Rational B-Splines (NURBS) [16–18] or T-splines [19,20], where the same set of basis functions is used to represent the solution region and conduct the numerical simulation of PDEs. The framework of IGA is proposed to develop the seamless integration between FEM and computer-aided design (CAD). Not only that, but it also has higher numerical accuracy than FEM, where we can easily implement the p-refinement, h-refinement, and even k-refinement by the technique of the knot insertion and/or order elevation. Therefore we can improve the accuracy of the numerical simulation without destroying the original geometric properties, which removes the interactive communication with the CAD system. Subdivision technology is compatible with NURBS, which has the capability of the refineability of B-spline techniques. Surface subdivision can construct smooth surfaces from arbitrary topological meshes by designing a set of simple and efficient refinement schemes [21,22]. Subdivision technology not only conveniently handles complicated geometric forms but also maintains original characteristics near boundaries through straightforward extensions, such as concave/convex angles and sharp/smooth creases. The discretization with single-patch NURBS-based IGA and implicit backward differentiation formula schemes was proposed to solve mean curvature (second-order) and Willmore (fourth-order) flows in [23]. Both Loop subdivision [24–27] and Catmull–Clark subdivision [28–30] have been utilized in IGA. Local refinement and convergence rate [31,32] are investigated in Catmull–Clark subdivision-based IGA. The subdivision-based IGA methodology can be viewed as the natural choice for higher-order FEM in engineering practice, see [26,27,33,34] as well.

Since this article aims to develop an accurate and efficient fully discrete strategy for solving the Allen–Cahn and Cahn–Hilliard models on curved surfaces with complex geometry. Hence, after we adopt the efficient subdivision-based IGA method for the spatial discretization, the remaining challenge becomes which method to use for time discretization. So far, we know that many successful methods exist to deal with the Allen–Cahn and Cahn–Hilliard equation, see [35–40]. However, as everyone knows, for the Allen–Cahn and Cahn–Hilliard equations, fully-implicit or explicit type discretization methods for the nonlinear terms will inevitably impose rigorous stable limitations for the time step due to the stiffness issue embedded in these equations, so they are inefficient in practice. To obtain an efficient fully discrete scheme on the surface that is not only easy to implement, but also has relatively high temporal accuracy, we adopt the subdivision-based IGA method for the space on the one hand, and the IEQ method, which is an efficient approach to construct the linear and energy stable scheme for phase-field models, see [39–44], for the time discretization on the other hand. We expect the combination of these two approaches will give us a satisfactory fully discrete numerical scheme on the complex curved surface.

We also note that when the IEQ method was originally developed in [35], it requires solving a linear system with variable coefficients at each time step. It is well-known that solving a system with variable coefficients takes more time than a linear system with only constant coefficients. Therefore, to reduce the disadvantage that the original IEQ method leads to higher computational cost, in this paper, we modify the IEQ method to the so-called explicit-IEQ (EIEQ, for short) method by introducing an auxiliary nonlocal variable and design a special type but trivial ODE for it, see also [45] for its application to different models. The new EIEQ method only requires us to solve some linear constant-coefficient equations with a completely decoupled structure, so it possesses very high efficiency in practice. We not only rigorously prove that our schemes possess the property of the unconditional energy stability, but also propose a decoupling strategy that only requires solving some constant-coefficient elliptic equations at each time step. Furthermore, in addition to some stability and accuracy tests, we implement several complex surface-based examples to illustrate the flexibility and robustness of the proposed scheme.

We organize the rest of this paper in the following way. In Section 2, we give a brief introduction to notations of surfaces, the Allen–Cahn and Cahn–Hilliard models on surfaces. In Section 3, the subdivision-based IGA method is introduced and a fully discrete scheme based on the EIEQ time advancing strategy is developed. The proof of unconditional energy stability is given, along with a strategy for how to realize the decoupled implementation. We provide various numerical examples to illustrate the accuracy and efficiency of the proposed scheme in Section 4. Section 5 gives some concluding remarks.

2. Model systems on the surfaces

2.1. Surface differential geometry

We first briefly introduce a mathematical framework of the surface which includes the parameterization and some differential geometric operators.

Let $\mathcal{S} := \{\mathbf{x}(u^1, u^2) \in \mathbb{R}^3 : (u^1, u^2) \in \mathscr{D} \subset \mathbb{R}^2\}$ be a sufficiently smooth and orientable surface. Now we can parameterize it. Denote $g_{\alpha\beta} = \langle \mathbf{x}_{u^\alpha}, \mathbf{x}_{u^\beta} \rangle$ and $b_{\alpha\beta} = \langle \mathbf{n}, \mathbf{x}_{u^\alpha u^\beta} \rangle$ be the coefficients of the first and the second fundamental forms of $\mathcal{S}$ with

$$\mathbf{x}_{u^\alpha} = \frac{\partial \mathbf{x}}{\partial u^\alpha}, \quad \mathbf{x}_{u^\alpha u^\beta} = \frac{\partial^2 \mathbf{x}}{\partial u^\alpha \partial u^\beta}, \quad \alpha, \beta = 1, 2,$$
$$\mathbf{n} = (\mathbf{x}_{u^1} \times \mathbf{x}_{u^2})/\|\mathbf{x}_{u^1} \times \mathbf{x}_{u^2}\|,$$

where $\langle \cdot, \cdot \rangle$, $\|\cdot\|$ and $\cdot \times \cdot$ stand for the usual inner product, Euclidean norm and cross product in $\mathbb{R}^3$ respectively. Then we introduce some notations as

$$[g^{\alpha\beta}] = [g_{\alpha\beta}]^{-1}, \; g = \det[g_{\alpha\beta}], \; [b^{\alpha\beta}] = [b_{\alpha\beta}]^{-1}, \; b = \det[b_{\alpha\beta}].$$

The matrix form of the *Weingarten map* is denoted as

$$\mathbf{S} = [b_{\alpha\beta}][g^{\alpha\beta}] = \frac{1}{g} \begin{bmatrix} b_{11}g_{22} - b_{12}g_{12} & b_{12}g_{11} - b_{11}g_{12} \\ b_{12}g_{22} - b_{22}g_{12} & b_{22}g_{11} - b_{12}g_{12} \end{bmatrix},$$

which is a self-adjoint linear map on the tangent space $T_{\mathbf{x}}\mathcal{S} := \operatorname{span}\{\mathbf{x}_{u^1}, \mathbf{x}_{u^2}\}$. Then the eigenvalues k_1 and k_2 of $\mathbf{S}$ are the *principal curvatures* of $\mathcal{S}$, whose arithmetic average and product are the *mean curvature* H and the *Gaussian curvature* K, namely,

$$H = \frac{k_1 + k_2}{2} = \frac{\operatorname{tr}(\mathbf{S})}{2} = \frac{b_{11}g_{22} - 2b_{12}g_{12} + b_{22}g_{11}}{2g}, \quad K = k_1 k_2 = \det(\mathbf{S}) = \frac{b_{11}b_{22} - b_{12}^2}{g},$$

respectively. The mean curvature normal is referred to $\mathbf{H} = H\mathbf{n}$. Some differential geometric operators of surface need to be introduced.

2.1.1. Tangential gradient operator

Denote $C^1(\mathcal{S})$ be a function space composing of C^1 smooth functions of $\mathcal{S}$. Considering $f \in C^1(\mathcal{S})$, the tangential gradient operator ∇_s acting on f is defined as

$$\nabla_s f = [\mathbf{x}_{u^1}, \mathbf{x}_{u^2}][g^{\alpha\beta}][f_{u^1}, f_{u^2}]^T \in \mathbb{R}^3. \tag{2.1}$$

For a vector-valued function $\mathbf{f} = [f_1, \ldots, f_k]^T \in C^1(\mathcal{S})^k$, the gradient ∇_s acting on $\mathbf{f}$ is defined as

$$\nabla_s \mathbf{f} = [\nabla_s f_1, \ldots, \nabla_s f_k] \in \mathbb{R}^{3\times k}.$$

2.1.2. Divergence operator

Let $\mathbf{v} \in [C^1(\mathcal{S})]^3$ be a smooth vector field on surface $\mathcal{S}$. Then the divergence operator div_s acting on $\mathbf{v}$ is defined as

$$\operatorname{div}_s(\mathbf{v}) = \frac{1}{\sqrt{g}} \left[\frac{\partial}{\partial u^1}, \frac{\partial}{\partial u^2}\right] \left[\sqrt{g}[g^{\alpha\beta}][\mathbf{x}_{u^1}, \mathbf{x}_{u^2}]^T \mathbf{v}\right]. \tag{2.2}$$

2.1.3. Laplace–Beltrami operator

Let $f \in C^2(\mathcal{S})$. Then the Laplace–Beltrami operator (LBO) Δ_s acting on f is defined as

$$\Delta_s f = \mathrm{div}_s(\nabla_s f).$$

With the definitions of Δ_s and div_s, we derive

$$\Delta_s f = \frac{1}{g}(g_{22} f_{11} + g_{11} f_{22} - 2 g_{12} f_{12}), \tag{2.3}$$

where $f_{\alpha\beta} = f_{u^\alpha u^\beta} - (\nabla_s f)^{\mathrm{T}} \mathbf{x}_{u^\alpha u^\beta}$, $\alpha, \beta = 1, 2$. The second-order differential operator Δ_s relates to the mean curvature vector, i.e., $\Delta_s \mathbf{x} = 2\mathbf{H}$.

2.2. Allen–Cahn and Cahn–Hilliard equations on the surface

Assuming that $\mathcal{S}$ is a sufficiently smooth surface, for a given constant k and a function $f \in C^\infty(\mathcal{S})$, we denote $\nabla^k f$ the kth order covariant derivative of function f, with the convention $\nabla^0 f = f$. Let

$$C_k(\mathcal{S}) = \left\{ f \in C^\infty(\mathcal{S}) : \int_s |\nabla^j f|^2 \mathrm{d}\mathbf{x} \leq \infty \text{ for } j = 0, \ldots, k \right\}. \tag{2.4}$$

It is obvious that $C_k(\mathcal{S}) = C^\infty(\mathcal{S}) \subset C^k(\mathcal{S}) \subset H^k(\mathcal{S})$. The Sobolev space $H^k(\mathcal{S})$ on the surface $\mathcal{S}$ is denoted as Definition 2.1.

Definition 2.1. Let $\mathcal{S}$ be a compact surface with at least kth order smoothness. Sobolev space $H^k(\mathcal{S})$ is the completion of $C_k(\mathcal{S})$ in the sense of norm

$$\|f\|_{H^k(\mathcal{S})} := \Big(\sum_{j=0}^{k} \int_s |\nabla^j f|^2 \mathrm{d}\mathbf{x} \Big)^{\frac{1}{2}}. \tag{2.5}$$

Two inner products on surface need to be introduced as

$$(u, v) = \int_s uv \, \mathrm{d}\mathbf{x}, \quad \text{and} \quad (\nabla_s u, \nabla_s v) = \int_s \nabla_s u \cdot \nabla_s v \, \mathrm{d}\mathbf{x}.$$

The Allen–Cahn and Cahn–Hilliard equations can be represented as L^2 and H^{-1} gradient flows of the following Liapunov energy functional respectively,

$$E(\phi) = \int_s \left(\frac{\epsilon^2}{2} |\nabla_s \phi|^2 + F(\phi) \right) \mathrm{d}\mathbf{x}, \tag{2.6}$$

where $\phi(\mathbf{x}, t)$ is to be solved scalar function on the surface $\mathcal{S}$, $\mathbf{x} \in \mathcal{S}$, $\epsilon \ll 1$ representing the interface width, and $F(\phi)$ is the nonlinear Ginzburg–Landau double-well type potential $F(\phi) = \frac{1}{4}(\phi^2 - 1)^2$.

The variation of the total free energy (2.6) in $L^2(\mathcal{S})$ results in the Allen–Cahn equation, that reads as:

$$\phi_t = \epsilon^2 \Delta_s \phi - f(\phi), \quad (\mathbf{x}, t) \in \mathcal{S} \times (0, T], \tag{2.7}$$

where $f(\phi) = F'(\phi)$. The initial condition is $\phi|_{t=0} = \phi_0$, and we only consider closed surface domains without any boundary conditions.

The variation of the total free energy (2.6) in $H^{-1}(\mathcal{S})$ results in the Cahn–Hilliard equation, that reads as:

$$\phi_t - \Delta_s w = 0, \tag{2.8}$$

$$w = -\epsilon^2 \Delta_s \phi + f(\phi), \quad (\mathbf{x}, t) \in \mathcal{S} \times (0, T], \tag{2.9}$$

where w is the chemical potential. The initial condition is $\phi|_{t=0} = \phi_0$. Similarly, we only consider closed surface domains without the boundary conditions.

It is well known that the Allen–Cahn and Cahn–Hilliard equations satisfy the following energy dissipation law,

$$\frac{d}{dt} E(\phi) \leq 0. \tag{2.10}$$

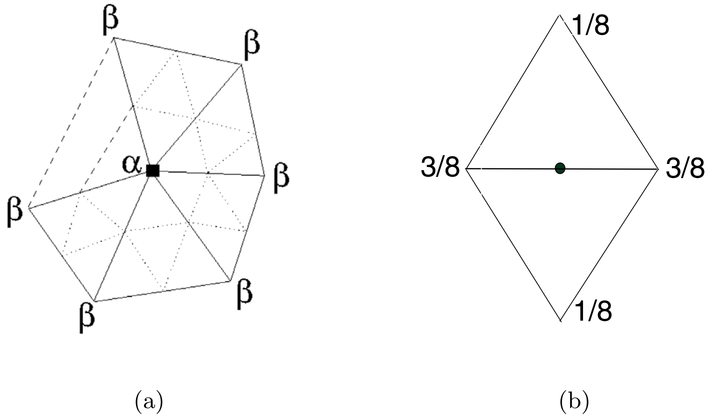

(a) (b)

Fig. 3.1. (a) Vertex refinement rule $\alpha = 1 - n\beta$, where $\beta = \frac{1}{n}\left[\frac{5}{8} - \left(\frac{3}{8} + \frac{1}{4}\cos\frac{2\pi}{n}\right)^2\right]$ and n is the valence of the control vertex; and (b) edge refinement rule.

3. IGA-EIEQ scheme on the surface

In this section, we aim to construct a fully discrete scheme to solve the Allen–Cahn Eq. (2.7) and the Cahn–Hilliard Eq. (2.8)–(2.9) on the surface. The method combines the recently developed IGA approach based on Loop subdivision [24,26,27] for the spatial discretization and the second-order EIEQ method as a time advancing strategy.

3.1. Subdivision-based IGA method

We now introduce the subdivision-based IGA method. Considering an initial control mesh with arbitrary topology, subdivision technology creates a smooth surface through an infinite refinement process, which includes the rules of recalculation of old vertex position and generation of new edge points (or face points). Considering the flexibility of triangular meshes, we adopt the Loop subdivision technique, which generalizes the quartic box splines for manifold triangle meshes. Any initial rough mesh can be used as a control mesh to define a subdivision limit surface. This initial control mesh is repeatedly refined by specified subdivision rules so that a series of increasingly refined meshes can be generated. The limit of this refinement process is a limit surface with C^1 smoothness. The limit surface is used to represent physical domains and perform numerical simulations to achieve a unified discretization of the PDEs on surfaces.

3.1.1. Loop subdivision schemes

A Loop subdivision scheme was proposed by Loop [22] for triangular control meshes. We can achieve a C^2 smooth surface by use of the Loop refinement process where the surface is C^1 smooth at a finite number of extraordinary control points on the initial rough mesh. It only needs two subdivision rules, including the recalculation of old points and the generation of new edge points, which can cause a triangle patch to be divided into four small triangle patches. The old control point with n valence is updated for itself with weight $\alpha = 1 - n\beta$ and its 1-ring surrounding neighborhood points with weight $\beta = \frac{1}{n}\left[\frac{5}{8} - \left(\frac{3}{8} + \frac{1}{4}\cos\frac{2\pi}{n}\right)^2\right]$ (see Fig. 3.1(a)). A new point on each edge is created through a simple weighted average algorithm shown in Fig. 3.1(b).

3.1.2. Evaluation of subdivision surfaces

An important element in the numerical treatments is the reliable and accurate evaluation of the limit surface to finish the finite element integrals which need to compute the Loop basis functions, derivatives of basis functions and inner products between them. Loop subdivision surface with any topology structure has no explicit formulation so that the computation at any point on Loop limit surface is a non-trivial work. Loop limit surface can be parameterized over its corresponding triangulation of control mesh, which implies a decomposition of the surface into triangular

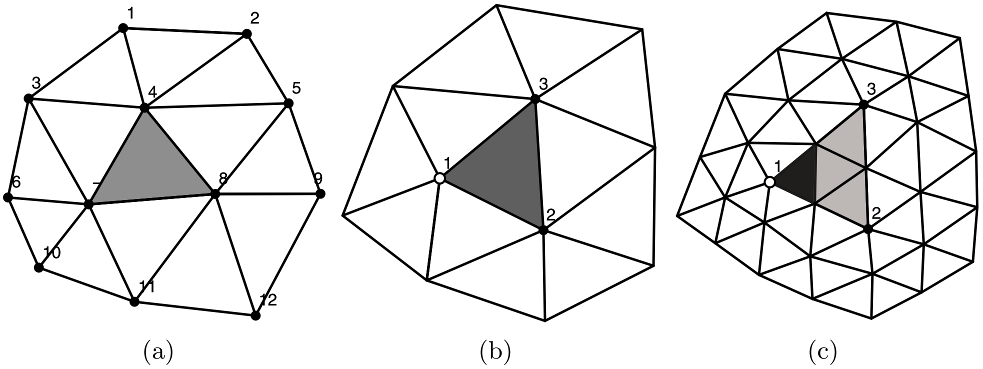

Fig. 3.2. (a) Computation of a regular Loop subdivision patch. The shaded domain is a quartic box-spline patch with its surrounding twelve control points; and (b) computation of an irregular Loop subdivision patch. The control point denoted as "1" is an extraordinary control point. Subdividing this patch once can generate three small quartic box-spline patches and one uncomputable patch. This uncomputable patch can be repeatedly subdivided to generate more quartic box-spline patches.

patches called limit patches. Each triangular limit patch on the control mesh can be used as a parametric region of triangular surface nesting on the limit surface. We have an explicit expression for the triangular loop surface patch with regular topology structure, which means the valence of the three control points for this patch must be six. Then a quartic box-spline expression can be used to compute the regular Loop subdivision surface patch, described as

$$\mathcal{S}(\mathbf{x}(u,v)) = \sum_{i=1}^{12} B_i(u,v)\mathbf{x}_i^k, \tag{3.1}$$

where we use $(u, v, 1-u-v)$ as the barycentric coordinates of the parametric limit patch, $\mathbf{x}_i^k$ are the corresponding 2-ring surrounding neighbor control points of the control mesh (See Fig. 3.2 (a)), and B_i are the quartic box-spline (See their analytic expression in [46]). We have no explicitly computable formula for the triangular loop surface patch with an irregular topology structure, which means the valence of at least one control point for this patch is not six. Fortunately, we can still use the quartic box-spline form (3.1) to calculate the resulting limit surface patch through a fast algorithm proposed by Stam [46]. The core idea is to subdivide repeatedly this patch until the position you need to calculate is included in a quartic box-spline patch (See Fig. 3.2(b)).

The Loop basis functions have the 2-ring of triangles surrounding the given control points as its natural support set. The evaluation of the limit surface can be performed at some fixed parameter points (Gauss points) within every limit patch. In the context of finite element simulations, we only need to ensure that the quadratures are computed to arrive at the necessary precision. Therefore, we only need to perform very limited subdivision steps to make all of the hierarchical limit patches become computable quartic box-splines patches. To reduce the computation cost, we develop a simplified and generalized approach for adaptive discretization subdivision, whose basic idea is to replace the refinement of mesh patches with the refinement of basis functions (see [27]).

3.1.3. Finite element space of loop subdivision

Based on an initial control mesh Ω_h^0 of Loop subdivision, the hierarchical control meshes are denoted as $\Omega_h^k,\ k = 0, \ldots, \infty$, where k denotes the subdivision level. We use $\mathcal{S}$ to denote the limit surface after doing the infinite subdivision process $k \to \infty$. As described in Section 3.1.1, considering a control point $\mathbf{x}_0^k$ of the mesh Ω_h^k whose valence is n, we denote its 1-ring neighboring control points as $\mathbf{x}_j^k,\ j = 1, 2, \ldots, n$. We can recalculate it by the formula $\mathbf{x}_0^{k+1} = (1-n\beta)\mathbf{x}_0^k + \beta\sum_{j=1}^{n}\mathbf{x}_j^k$ which is converged under the condition of the parameter $\beta \in (-3/8n, 13/8n)$. There exists an explicit expression about the limit position of each point on the control mesh described in Lemma 3.1.

Lemma 3.1. *Consider a control point $\mathbf{x}_0^k$ of the triangular mesh Ω_h^k, where its valence is n, and denote $\mathbf{x}_j^k$, $j = 1, \ldots, n$, be its 1-ring neighboring control points. All these control points converge to a single position*

$$\hat{\mathbf{x}}_0 = (1 - nl)\mathbf{x}_0^k + l \sum_{j=1}^{n} \mathbf{x}_j^k, \qquad l = \frac{1}{n + 3/(8\beta)}, \tag{3.2}$$

as the subdivision step $k \to \infty$ (see [22] for the proof).

Our finite element function space is defined by the limit process based on the Loop subdivision approach. This function space is used to describe the solution surface area with any topology structure and perform the evolution of the phase-field functions defined on the solution surface area. The methodology of using loop subdivision to represent the solution surface area with any topology structure is consistent with the concept of the IGA strategy. The triangulation form of the limit surface $\mathcal{S}$ is denoted as $\mathcal{S}_h$ where h denotes the mesh size. The triangular mesh $\mathcal{S}_h = \bigcup_{\alpha=1}^{k} e_\alpha, \mathring{e}_\alpha \bigcap \mathring{e}_\beta = \emptyset$ for $\alpha \neq \beta$, where $\mathring{e}_\alpha$ is within the triangular patch e_α. About each patch e_α, it needs to be parameterized as

$$\mathbf{x}_\alpha : \quad \mathsf{e} \to e_\alpha; \quad (u, v) \ \mapsto \ \mathbf{x}_\alpha(u, v),$$

where the parametric element $\mathsf{e} = \{(u, v) : 0 \le u \le 1, 0 \le v \le 1\}$, u and v are its barycentric coordinates. The domain area e_α of $\mathcal{S}_h$ can always be calculated by the explicit formula of the quartic box-spline.

We denote the set of basis functions $\phi_1, \ldots, \phi_n$ for the finite element function space $H^2(\mathcal{S}_h)$ where the control mesh $\mathcal{S}_h$ has n control points $\mathbf{x}_1, \cdots, \mathbf{x}_n$. As described above, our basis functions result from the limit process based on Loop subdivision approach. The solution surface $\mathcal{S}$ is exactly represented as the limit form through the Loop subdivision scheme,

$$\mathcal{S}(\mathbf{x}(u, v)) = \mathcal{S}(x(u, v), y(u, v), z(u, v)) = \sum_{j=1}^{n} \phi_j(u, v)\mathbf{x}_j. \tag{3.3}$$

This kind of the basis functions also have the superior properties of classical finite elements. Firstly, they are nonnegative everywhere and positive around their corresponding control point because the weight coefficients of the subdivision schemes are positive. Secondly, because the limit value at each control point $\mathbf{x}_j$ is a linear summation of itself and its one-ring neighboring control points, the support of each basis function has two-ring neighborhoods. Finally, the weight coefficients of all subdivision schemes are summed to one, therefore we have $\sum_{j=0}^{m} \phi_j = 1$.

3.2. EIEQ time advancing strategy

The goal of the time-advance strategy is to develop a linear, easy-to-implement, unconditionally energy stable scheme for the PDE system. Although the second-order Allen–Cahn system (2.7) and the fourth-order Cahn–Hilliard system (2.8)–(2.9) have different forms, it is well known that the challenge to achieve this goal is the same, that is, find an appropriate discrete format about the nonlinear term $f(\phi)$. The procedure of using the EIEQ method is to design some new auxiliary variables, where one variable is used to "quadratize" the nonlinear functional $F(\phi)$, and the other is used to realize the decoupling type calculation. In this way, a linear and second-order time accurate scheme with the property of unconditional energy stability can be obtained and one only needs to solve a few elliptic constant-coefficient models with the decoupled structure at each time step, thus achieving very efficient computation. We present the details as follows.

Since the double-well functional $F(\phi)$ is bounded from below, we define the first auxiliary variable $U(\phi)$ by the following formulation

$$U(\phi) = \sqrt{F(\phi) - \frac{S}{2}\phi^2 + B}, \tag{3.4}$$

where $S, B > 0$ are two fixed constants. Note that the negative quadratic term related to S can be always bounded by $F(\phi)$ from below since $F(\phi)$ is a fourth-order polynomial with a positive leading coefficient. The benefit of adding the positive constant B is to guarantee the term in the square root is always positive. We denote

$$H = 2\frac{d}{d\phi}U(\phi) = \frac{f(\phi) - S\phi}{\sqrt{F(\phi) - \frac{S}{2}\phi^2 + B}}. \tag{3.5}$$

We further define the second nonlocal auxiliary variable $Q(t)$, and a special ODE for it, that reads as

$$\begin{cases} Q_t = (HU, \phi_t) - (H\phi_t, U), \\ Q|_{t=0} = 1. \end{cases} \tag{3.6}$$

Obviously $Q_t = 0$ and $Q|_{(t=0)} = 1$, so that $Q(t) = 1$.

Using these two newly defined terms U and Q, taking the time derivative of (3.4) and merging (3.6), the Allen–Cahn system (2.7) is rewritten as:

$$\phi_t = \epsilon^2 \Delta_s \phi - S\phi - QHU, \tag{3.7}$$

$$U_t = \frac{1}{2} QH\phi_t, \tag{3.8}$$

$$Q_t = (HU, \phi_t) - (H\phi_t, U), \tag{3.9}$$

where the initial condition $\phi|_{t=0} = \phi_0$, $U|_{t=0} = \sqrt{F(\phi_0) - \frac{S}{2}\phi_0^2 + B}$.

The new transformation system (3.7)–(3.9) is actually completely equivalent to the original system. This can be easily deduced by integrating the ODE (3.8) over time and noting that $Q = 1$. This new system also retains the law of energy dissipation described in Theorem 3.1.

Theorem 3.1. *The transformed equivalent system (3.7)–(3.9) holds the law of the energy dissipation as*

$$\frac{d}{dt} E(\phi, Q, U) = -\|\phi_t\|^2 \le 0, \tag{3.10}$$

where

$$E(\phi, Q, U) = \int_s \left(\frac{\epsilon^2}{2} |\nabla_s \phi|^2 + \frac{S}{2} |\phi|^2 + |U|^2 - B \right) \mathrm{dx} + \frac{1}{2}|Q|^2 - \frac{1}{2}. \tag{3.11}$$

Proof. By taking the L^2 inner product of (3.7) with ϕ_t, of (3.8) with $2U$, of (3.9) with Q, and perform the integration by parts, we get

$$(\phi_t, \phi_t) = -\epsilon^2 (\nabla_s \phi, \nabla_s \phi_t) - S(\phi, \phi_t) - Q(HU, \phi_t), \tag{3.12}$$

$$\frac{d}{dt} \int_s |U|^2 d\mathrm{x} = Q(H\phi_t, U), \tag{3.13}$$

$$\frac{d}{dt} \left(\frac{1}{2} |Q|^2 \right) = Q(HU, \phi_t) - Q(H\phi_t, U). \tag{3.14}$$

Combining (3.12)–(3.14), we gain the law of the energy dissipation (3.10). □

For the Cahn–Hilliard system (2.8)–(2.9), we implement the similar procedure, thus it can be rewritten as:

$$\phi_t - \Delta_s w = 0, \tag{3.15}$$

$$w = -\epsilon^2 \Delta_s \phi + S\phi + QHU, \tag{3.16}$$

$$U_t = \frac{1}{2} QH\phi_t, \tag{3.17}$$

$$Q_t = (HU, \phi_t) - (H\phi_t, U), \tag{3.18}$$

where H and Q are defined as in (3.5) and (3.6) respectively, and the initial condition $\phi|_{t=0} = \phi_0$, $U|_{t=0} = \sqrt{F(\phi_0) - \frac{S}{2}\phi_0^2 + B}$.

The new transformed system (3.15)–(3.18) also follows the law of the energy dissipation, which is given as follows.

Theorem 3.2. *The transformed equivalent system (3.15)–(3.18) holds the law of the energy dissipation as*

$$\frac{d}{dt} E(\phi, Q, U) = -\|\nabla_s w\|^2 \le 0, \tag{3.19}$$

where

$$E(\phi, Q, U) = \int_s \left(\frac{\epsilon^2}{2}|\nabla_s \phi|^2 + \frac{S}{2}|\phi|^2 + |U|^2 - B\right) \mathrm{dx} + \frac{1}{2}|Q|^2 - \frac{1}{2}. \tag{3.20}$$

Proof. By taking the L^2 inner product of (3.15) with w, of (3.16) with $-\phi_t$, of (3.17) with $2U$, of (3.18) with Q, and performing the integration by parts, we get

$$(\phi_t, w) = -(\nabla_s w, \nabla_s w), \tag{3.21}$$

$$-(w, \phi_t) = -\epsilon^2(\nabla_s \phi, \nabla_s \phi_t) - S(\phi, \phi_t) - Q(HU, \phi_t), \tag{3.22}$$

$$\frac{d}{dt}\int_s |U|^2 dx = Q(H\phi_t, U), \tag{3.23}$$

$$\frac{d}{dt}\left(\frac{1}{2}|Q|^2\right) = Q(HU, \phi_t) - Q(H\phi_t, U). \tag{3.24}$$

Combining (3.21)–(3.24), we obtain the law of the energy dissipation (3.19). □

3.3. Fully discrete schemes

In this subsection, the fully discrete schemes for solving the Allen–Cahn system (3.7)–(3.9) and the Cahn–Hilliard system (3.15)–(3.17) are given. We also prove their unconditional energy stability, and also design a decoupling implementation process for them. In what follows, denote the time step size as $\delta t > 0$ and $t^n = n\delta t$ for $0 \le n \le N = [T/\delta t]$. Take the test functions θ_h, ϑ_h and $\zeta_h \in H^2(\mathcal{S}_h)$, which is our IGA finite element space induced by the limit form of Loop subdivision as described in Section 3.1.

3.3.1. Allen–Cahn system

Assuming that ϕ_h^n, U_h^n, Q^n and ϕ_h^{n-1}, U_h^{n-1}, Q^{n-1} are known, we compute ϕ_h^{n+1}, U_h^{n+1}, Q^{n+1} by the following fully-discrete, second-order backward difference formula (BDF2) numerical scheme:

$$\left(\frac{3\phi_h^{n+1} - 4\phi_h^n + \phi_h^{n-1}}{2\delta t}, \theta_h\right) = -\epsilon^2(\nabla_s \phi_h^{n+1}, \nabla_s \theta_h) - S(\phi_h^{n+1}, \theta_h) - Q^{n+1}(H_h^* U_h^*, \theta_h), \tag{3.25}$$

$$\left(\frac{3U_h^{n+1} - 4U_h^n + U_h^{n-1}}{2\delta t}, \zeta_h\right) = \frac{1}{2}Q^{n+1}\left(H_h^* \phi_{ht}^*, \zeta_h\right), \tag{3.26}$$

$$\frac{3Q^{n+1} - 4Q^n + Q^{n-1}}{2\delta t} = (H_h^* U_h^*, \frac{3\phi_h^{n+1} - 4\phi_h^n + \phi_h^{n-1}}{2\delta t}) - (H_h^* \phi_{ht}^*, U_h^{n+1}), \tag{3.27}$$

where

$$\begin{cases} \phi_h^* = 2\phi_h^n - \phi_h^{n-1}, \ U_h^* = 2U_h^n - U_h^{n-1}, \\ H_h^* = H(\phi_h^*), \ \phi_{ht}^* = \dfrac{5\phi_h^n - 8\phi_h^{n-1} + 3\phi_h^{n-2}}{2\delta t}. \end{cases} \tag{3.28}$$

The unconditional energy stability of the scheme (3.25)–(3.27) is shown as below.

Theorem 3.3. *The second-order scheme (3.25)–(3.27) is unconditionally energy stable, i.e., satisfies the following discrete energy dissipation law:*

$$E_{ac}^{n+1} - E_{ac}^n \le -\delta t \| \frac{3\phi_h^{n+1} - 4\phi_h^n + \phi_h^{n-1}}{2\delta t} \|^2, \tag{3.29}$$

where, for an integer $k \ge 0$, the discrete energy E_{ac}^k is defined as

$$\begin{aligned} E_{ac}^k = &\frac{\epsilon^2}{4}(\|\nabla_s \phi_h^k\|^2 + \|2\nabla_s \phi_h^k - \nabla_s \phi_h^{k-1}\|^2) + \frac{S}{4}(\|\phi_h^k\|^2 + \|2\phi_h^k - \phi_h^{k-1}\|^2) \\ &+ \frac{1}{2}(\|U_h^k\|^2 + \|2U_h^k - U_h^{k-1}\|^2) + \frac{1}{4}(|Q^k|^2 + |2Q^k - Q^{k-1}|^2) - B|\mathcal{S}| - \frac{1}{2}. \end{aligned} \tag{3.30}$$

Proof. By taking $\theta_h = \frac{3\phi_h^{n+1}-4\phi_h^n+\phi_h^{n-1}}{2\delta t}$ in (3.25) and performing the integration by parts, we derive

$$\begin{aligned}\delta t \| \frac{3\phi_h^{n+1}-4\phi_h^n+\phi_h^{n-1}}{2\delta t} \|^2 = &- \frac{\epsilon^2}{4}(\|\nabla_s\phi_h^{n+1}\|^2 - \|\nabla_s\phi_h^n\|^2 + \|2\nabla_s\phi_h^{n+1} - \nabla_s\phi_h^n\|^2 \\ &- \|2\nabla_s\phi_h^n - \nabla_s\phi_h^{n-1}\|^2 + \|\nabla_s\phi_h^{n+1} - 2\nabla_s\phi_h^n + \nabla_s\phi_h^{n-1}\|^2) \\ &- \frac{S}{4}(\|\phi_h^{n+1}\|^2 - \|\phi_h^n\|^2 + \|2\phi_h^{n+1} - \phi_h^n\|^2 \\ &- \|2\phi_h^n - \phi_h^{n-1}\|^2 + \|\phi_h^{n+1} - 2\phi_h^n + \phi_h^{n-1}\|^2) \\ &- Q^{n+1}(H_h^* U_h^*, \frac{3\phi_h^{n+1}-4\phi_h^n+\phi_h^{n-1}}{2}),\end{aligned} \tag{3.31}$$

where the following identity is used:

$$2(3a-4b+c, a) = a^2 - b^2 + (2a-b)^2 - (2b-c)^2 + (a-2b+c)^2. \tag{3.32}$$

By taking $\zeta_h = 2\delta t U_h^{n+1}$ in (3.26) and using (3.32), we have

$$\begin{aligned}&\frac{1}{2}(\|U_h^{n+1}\|^2 - \|U_h^n\|^2 + \|2U_h^{n+1} - U_h^n\|^2 - \|2U_h^n - U_h^{n-1}\|^2 \\ &\qquad + \|U_h^{n+1} - 2U_h^n + U_h^{n-1}\|^2) = \delta t Q^{n+1}(H_h^*\phi_{ht}^*, U_h^{n+1}).\end{aligned} \tag{3.33}$$

By multiplying (3.27) with $\delta t Q^{n+1}$ and using (3.32), we have

$$\begin{aligned}&\frac{1}{4}(|Q^{n+1}|^2 - |Q^n|^2 + |2Q^{n+1} - Q^n|^2 - |2Q^n - Q^{n-1}|^2 + |Q^{n+1} - 2Q^n + Q^{n-1}|^2) \\ &= Q^{n+1}(H_h^* U_h^*, \frac{3\phi_h^{n+1}-4\phi_h^n+\phi_h^{n-1}}{2}) - \delta t Q^{n+1}(H_h^*\phi_{ht}^*, U_h^{n+1}).\end{aligned} \tag{3.34}$$

By combining (3.31), (3.33) and (3.34), we get

$$\begin{aligned}&\frac{\epsilon^2}{4}(\|\nabla_s\phi_h^{n+1}\|^2 - \|\nabla_s\phi_h^n\|^2 + \|2\nabla_s\phi_h^{n+1} - \nabla_s\phi_h^n\|^2 - \|2\nabla_s\phi_h^n - \nabla_s\phi_h^{n-1}\|^2 \\ &+\|\nabla_s\phi_h^{n+1} - 2\nabla_s\phi_h^n + \nabla_s\phi_h^{n-1}\|^2) \\ &+\frac{S}{4}(\|\phi_h^{n+1}\|^2 - \|\phi_h^n\|^2 + \|2\phi_h^{n+1} - \phi_h^n\|^2 - \|2\phi_h^n - \phi_h^{n-1}\|^2 + \|\phi_h^{n+1} - 2\phi_h^n + \phi_h^{n-1}\|^2) \\ &+\frac{1}{2}(\|U_h^{n+1}\|^2 - \|U_h^n\|^2 + \|2U_h^{n+1} - U_h^n\|^2 - \|2U_h^n - U_h^{n-1}\|^2 + \|U_h^{n+1} - 2U_h^n + U_h^{n-1}\|^2) \\ &+\frac{1}{4}(|Q^{n+1}|^2 - |Q^n|^2 + |2Q^{n+1} - Q^n|^2 - |2Q^n - Q^{n-1}|^2 + |Q^{n+1} - 2Q^n + Q^{n-1}|^2) \\ &= -\delta t \| \frac{3\phi_h^{n+1}-4\phi_h^n+\phi_h^{n-1}}{2\delta t} \|^2,\end{aligned}$$

which implies the energy stability (3.29) after we ignore some positive terms. □

3.3.2. Cahn–Hilliard system

Assuming that ϕ_h^n, w_h^n, U_h^n, Q^n and ϕ_h^{n-1}, w_h^{n-1}, U_h^{n-1}, Q^{n-1} are known, we compute ϕ_h^{n+1}, w_h^{n+1}, U_h^{n+1}, Q^{n+1} by the following fully-discrete scheme:

$$\left(\frac{3\phi_h^{n+1}-4\phi_h^n+\phi_h^{n-1}}{2\delta t}, \theta_h\right) = -(\nabla_s w_h^{n+1}, \nabla_s\theta_h), \tag{3.35}$$

$$(w_h^{n+1}, \vartheta_h) = \epsilon^2(\nabla_s\phi_h^{n+1}, \nabla_s\vartheta_h) + S(\phi_h^{n+1}, \vartheta_h) + Q^{n+1}(H_h^* U_h^*, \vartheta_h), \tag{3.36}$$

$$\left(\frac{3U_h^{n+1}-4U_h^n+U_h^{n-1}}{2\delta t}, \zeta_h\right) = \frac{1}{2}Q^{n+1}\left(H_h^*\phi_{ht}^*, \zeta_h\right), \tag{3.37}$$

$$\frac{3Q^{n+1}-4Q^{n}+Q^{n-1}}{2\delta t}=(H_h^*U_h^*,\frac{3\phi_h^{n+1}-4\phi_h^{n}+\phi_h^{n-1}}{2\delta t})-(H_h^*\phi_{ht}^*,U_h^{n+1}),\tag{3.38}$$

where ϕ_h^*, H_h^* and ϕ_{ht}^* are the same definition as (3.28).

The unconditional energy stability is shown below.

Theorem 3.4. *The second-order scheme (3.35)–(3.38) is unconditionally energy stable, i.e., satisfies the following discrete energy dissipation law:*

$$E_{ch}^{n+1}-E_{ch}^{n}\le-\delta t\|\nabla_s w_h^{n+1}\|^2,\tag{3.39}$$

where, for an integer $k\ge 0$, the discrete energy E_{ch}^k is defined as

$$\begin{aligned}E_{ch}^k=&\frac{\epsilon^2}{4}(\|\nabla_s\phi_h^k\|^2+\|2\nabla_s\phi_h^k-\nabla_s\phi_h^{k-1}\|^2)+\frac{S}{4}(\|\phi_h^k\|^2+\|2\phi_h^k-\phi_h^{k-1}\|^2)\\&+\frac{1}{2}(\|U_h^k\|^2+\|2U_h^k-U_h^{k-1}\|^2)+\frac{1}{4}(|Q^k|^2+|2Q^k-Q^{k-1}|^2)-B|\mathcal{S}|-\frac{1}{2}.\end{aligned}\tag{3.40}$$

Proof. By taking $\theta_h=-\delta t w_h^{n+1}$ in (3.35) and performing the integration by parts, we get

$$-\left(\frac{3\phi_h^{n+1}-4\phi_h^{n}+\phi_h^{n-1}}{2},w_h^{n+1}\right)=\delta t\|\nabla_s w_h^{n+1}\|^2.\tag{3.41}$$

By taking $\vartheta_h=\frac{3\phi_h^{n+1}-4\phi_h^{n}+\phi_h^{n-1}}{2}$ in (3.36) and using (3.32), we derive

$$\begin{aligned}\left(w_h^{n+1},\frac{3\phi_h^{n+1}-4\phi_h^{n}+\phi_h^{n-1}}{2}\right)=&\frac{\epsilon^2}{4}(\|\nabla_s\phi_h^{n+1}\|^2-\|\nabla_s\phi_h^{n}\|^2+\|2\nabla_s\phi_h^{n+1}-\nabla_s\phi_h^{n}\|^2\\&-\|2\nabla_s\phi_h^{n}-\nabla_s\phi_h^{n-1}\|^2+\|\nabla_s\phi_h^{n+1}-2\nabla_s\phi_h^{n}+\nabla_s\phi_h^{n-1}\|^2)\\&+\frac{S}{4}(\|\phi_h^{n+1}\|^2-\|\phi_h^{n}\|^2+\|2\phi_h^{n+1}-\phi_h^{n}\|^2\\&-\|2\phi_h^{n}-\phi_h^{n-1}\|^2+\|\phi_h^{n+1}-2\phi_h^{n}+\phi_h^{n-1}\|^2)\\&+Q^{n+1}(H_h^*U_h^*,\frac{3\phi_h^{n+1}-4\phi_h^{n}+\phi_h^{n-1}}{2}).\end{aligned}\tag{3.42}$$

By taking $\zeta_h=2\delta t U_h^{n+1}$ in (3.37) and using (3.32), we get

$$\begin{aligned}&\frac{1}{2}(\|U_h^{n+1}\|^2-\|U_h^{n}\|^2+\|2U_h^{n+1}-U_h^{n}\|^2-\|2U_h^{n}-U_h^{n-1}\|^2\\&\qquad+\|U_h^{n+1}-2U_h^{n}+U_h^{n-1}\|^2)=\delta t Q^{n+1}(H_h^*\phi_{ht}^*,U_h^{n+1}).\end{aligned}\tag{3.43}$$

By multiplying (3.38) with $\delta t Q^{n+1}$ and using (3.32), we obtain

$$\begin{aligned}\frac{1}{2}(3Q^{n+1}-4Q^{n}+Q^{n-1})Q^{n+1}=&Q^{n+1}(H_h^*U_h^*,\frac{3\phi_h^{n+1}-4\phi_h^{n}+\phi_h^{n-1}}{2})\\&-\delta t Q^{n+1}(H_h^*\phi_{ht}^*,U_h^{n+1}).\end{aligned}\tag{3.44}$$

By combining (3.41), (3.42), (3.43) and (3.44), and using (3.32), we deduce

$$\begin{aligned}&\frac{\epsilon^2}{4}(\|\nabla_s\phi_h^{n+1}\|^2-\|\nabla_s\phi_h^{n}\|^2+\|2\nabla_s\phi_h^{n+1}-\nabla_s\phi_h^{n}\|^2-\|2\nabla_s\phi_h^{n}-\nabla_s\phi_h^{n-1}\|^2\\&+\|\nabla_s\phi_h^{n+1}-2\nabla_s\phi_h^{n}+\nabla_s\phi_h^{n-1}\|^2)\\&+\frac{S}{4}(\|\phi_h^{n+1}\|^2-\|\phi_h^{n}\|^2+\|2\phi_h^{n+1}-\phi_h^{n}\|^2-\|2\phi_h^{n}-\phi_h^{n-1}\|^2+\|\phi_h^{n+1}-2\phi_h^{n}+\phi_h^{n-1}\|^2)\\&+\frac{1}{2}(\|U_h^{n+1}\|^2-\|U_h^{n}\|^2+\|2U_h^{n+1}-U_h^{n}\|^2-\|2U_h^{n}-U_h^{n-1}\|^2+\|U_h^{n+1}-2U_h^{n}+U_h^{n-1}\|^2)\end{aligned}$$

$$+\frac{1}{4}(|Q^{n+1}|^2 - |Q^n|^2 + |2Q^{n+1} - Q^n|^2 - |2Q^n - Q^{n-1}|^2 + |Q^{n+1} - 2Q^n + Q^{n-1}|^2)$$
$$= -\delta t\|\nabla_s w_h^{n+1}\|^2,$$

which implies the energy stability (3.39) after we ignore some positive terms. □

3.3.3. Decoupled scheme by the nonlocal splitting skill

The two developed schemes, (3.25)–(3.27) and (3.35)–(3.38), appear to be fully coupled. However, we can achieve fully decoupled type computation through a non-local splitting approach, which is described below.

Allen–Cahn system

Step 1: We split ϕ_h^{n+1} and U_h^{n+1} into a linear combination form as

$$\phi_h^{n+1} = \phi_{1h}^{n+1} + Q^{n+1}\phi_{2h}^{n+1}, \ U_h^{n+1} = U_{1h}^{n+1} + Q^{n+1}U_{2h,}^{n+1} \tag{3.45}$$

then we solve ϕ_{ih}^{n+1} and U_{ih}^{n+1}, $i = 1, 2$ as follows.

Using (3.45), we replace ϕ_h^{n+1} in the system (3.25)–(3.26), and decompose the obtained equations according to Q^{n+1} into the following four systems:

$$(\frac{3\phi_{1h}^{n+1} - 4\phi_h^n + \phi_h^{n-1}}{2\delta t}, \theta_h) = -\epsilon^2(\nabla_s\phi_{1h}^{n+1}, \nabla_s\theta_h) - S(\phi_{1h}^{n+1}, \theta_h), \tag{3.46}$$

$$(\frac{3\phi_{2h}^{n+1}}{2\delta t}, \theta_h) = -\epsilon^2(\nabla_s\phi_{2h}^{n+1}, \nabla_s\theta_h) - S(\phi_{2h}^{n+1}, \theta_h) - (H_h^*U_h^*, \theta_h), \tag{3.47}$$

$$(\frac{3U_{1h}^{n+1}}{2\delta t}, \zeta_h) = (\frac{4U_h^n - U_h^{n-1}}{2\delta t}, \zeta_h), \tag{3.48}$$

$$(\frac{3U_{2h}^{n+1}}{2\delta t}, \zeta_h) = \frac{1}{2}(H_h^*\phi_{ht}^*, \zeta_h). \tag{3.49}$$

All the above equations are completely independent. (3.46) and (3.47) can be easily solved because they are linear elliptic with constant coefficients, and (3.48) and (3.49) are just algebraic equations thus they can also easily be solved.

Step 2: By use of the known ϕ_h^{n+1} and U_h^{n+1} obtained by solving (3.46)–(3.49), we update Q^{n+1} in (3.38) through

$$\left(\frac{3}{2\delta t} - \eta_2\right) Q^{n+1} = \frac{1}{2\delta t}(4Q^n - Q^{n-1}) + \eta_1, \tag{3.50}$$

where η_1 and η_2 are given as

$$\begin{cases} \eta_1 = (H_h^*U_h^*, \dfrac{3\phi_{1h}^{n+1} - 4\phi_h^n + \phi_h^{n-1}}{2\delta t}) - (H_h^*\phi_{ht}^*, U_{1h}^{n+1}), \\ \eta_2 = (H_h^*U_h^*, \dfrac{3\phi_{2h}^{n+1}}{2\delta t}) - (H_h^*\phi_{ht}^*, U_{2h}^{n+1}), \end{cases} \tag{3.51}$$

and H_h^*, U_h^* and ϕ_{ht}^* are given in (3.28).

We need to prove the solvability of (3.50) through showing the coefficient $\frac{3}{2\delta t} - \eta_2 \neq 0$. Firstly by taking $\theta_h = \frac{3}{2\delta t}\phi_{2h}^{n+1}$ in (3.47), we get

$$\left\|\frac{3\phi_{2h}^{n+1}}{2\delta t}\right\|^2 + \frac{3\epsilon^2}{2\delta t}\left\|\nabla_s\phi_{2h}^{n+1}\right\|^2 + \frac{3S}{2\delta t}\left\|\phi_{2h}^{n+1}\right\|^2 = -(H_h^*U_h^*, \frac{3\phi_{2h}^{n+1}}{2\delta t}), \tag{3.52}$$

we then choose $\zeta_h = 2U_{2h}^{n+1}$ in (3.49) to achieve

$$\left\|\frac{3U_{2h}^{n+1}}{\delta t}\right\|^2 = (H_h^*\phi_h^*, U_{2h}^{n+1}). \tag{3.53}$$

We can get $-\eta_2 \geq 0$ by combining (3.52) and (3.53). Thus (3.50) is always solvable.

Cahn–Hilliard system:

Step 1: We split ϕ_h^{n+1}, w_h^{n+1} and U_h^{n+1} into a linear combination form as

$$\phi_h^{n+1} = \phi_{1h}^{n+1} + Q^{n+1}\phi_{2h}^{n+1},\ w_h^{n+1} = w_{1h}^{n+1} + Q^{n+1}w_{2h}^{n+1},\ U_h^{n+1} = U_{1h}^{n+1} + Q^{n+1}U_{2h,}^{n+1} \tag{3.54}$$

then we solve ϕ_{ih}^{n+1}, w_{ih}^{n+1} and U_{ih}^{n+1}, $i = 1, 2$ as follows.

Using (3.54), we replace ϕ_h^{n+1}, w_h^{n+1} and U_h^{n+1} in the system (3.35)–(3.37), and decompose the obtained equations according to Q^{n+1} into the following four systems:

$$\begin{cases} (\dfrac{3\phi_{1h}^{n+1} - 4\phi_h^n + \phi_h^{n-1}}{2\delta t}, \theta_h) = -(\nabla_s w_{1h}^{n+1}, \nabla_s \theta_h), \\ (w_{1h}^{n+1}, \vartheta_h) = \epsilon^2(\nabla_s \phi_{1h}^{n+1}, \nabla_s \vartheta_h) + S(\phi_{1h}^{n+1}, \vartheta_h), \end{cases} \tag{3.55}$$

$$\begin{cases} (\dfrac{3\phi_{2h}^{n+1}}{2\delta t}, \theta_h) = -(\nabla_s w_{2h}^{n+1}, \nabla_s \theta_h), \\ (w_{2h}^{n+1}, \vartheta_h) = \epsilon^2(\nabla_s \phi_{2h}^{n+1}, \nabla_s \vartheta_h) + S(\phi_{2h}^{n+1}, \vartheta_h) + (H_h^* U_h^*, \vartheta_h), \end{cases} \tag{3.56}$$

$$(\frac{3U_{1h}^{n+1}}{2\delta t}, \zeta_h) = (\frac{4U_h^n - U_h^{n-1}}{2\delta t}, \zeta_h), \tag{3.57}$$

$$(\frac{3U_{2h}^{n+1}}{2\delta t}, \zeta_h) = \frac{1}{2}(H_h^* \phi_{ht}^*, \zeta_h). \tag{3.58}$$

It can be seen the above systems are all independent, and (3.55)–(3.56) are linear elliptic and only have constant coefficients.

Step 2: We update Q^{n+1} in (3.38) through the same **Step 2** of solving the Allen–Cahn system.

Similarly, we need to prove the solvability of Q in (3.50) through showing the coefficient $\frac{3}{2\delta t} - \eta_2 \neq 0$. By taking $\theta_h = w_{2h}^{n+1}$ and $\vartheta_h = \frac{3}{2\delta t}\phi_{2h}^{n+1}$ in (3.56), we get

$$\left\|\nabla_s w_{2h}^{n+1}\right\|^2 + \frac{3\epsilon^2}{2\delta t}\left\|\nabla_s \phi_{2h}^{n+1}\right\|^2 + \frac{3S}{2\delta t}\left\|\phi_{2h}^{n+1}\right\|^2 = -(H_h^* U_h^*, \frac{3\phi_{2h}^{n+1}}{2\delta t}), \tag{3.59}$$

then choosing $\zeta_h = 2U_{2h}^{n+1}$ in (3.58), we obtain

$$\left\|\frac{3U_{2h}^{n+1}}{\delta t}\right\|^2 = (H_h^* \phi_h^*, U_{2h}^{n+1}). \tag{3.60}$$

We can get $-\eta_2 \geq 0$ by combining (3.59) and (3.60). Thus (3.50) is always solvable.

Through the above decoupling process, the calculation of all variables are fully decoupled, and all schemes only have constant coefficients, yielding very efficient computations in practice.

4. Numerical implementation

In this section, we carry out some numerical simulations to validate the accuracy, efficiency, and energy stability of the proposed schemes. The solution surface regions for numerical experiments result from the limit process of the proposed Loop subdivision. Similar to the classical FEM, the Gaussian integral calculation is carried out on each patch of the triangular discretization for the limit surface. The linear systems of the full discretization schemes for these two equations are highly sparse, we need a robust iterative method to solve them. In this paper, we adopt the GMRES solver, where we set the number of the iterative steps long enough to obtain proper convergence of the proposed schemes.

4.1. Convergence test

In the first numerical test, we verify the convergence rates of the developed numerical schemes. We consider the surface of a unit sphere, i.e.,

$$\mathcal{S} = \{(x, y, z) : \sqrt{x^2 + y^2 + z^2} = 1\}. \tag{4.1}$$

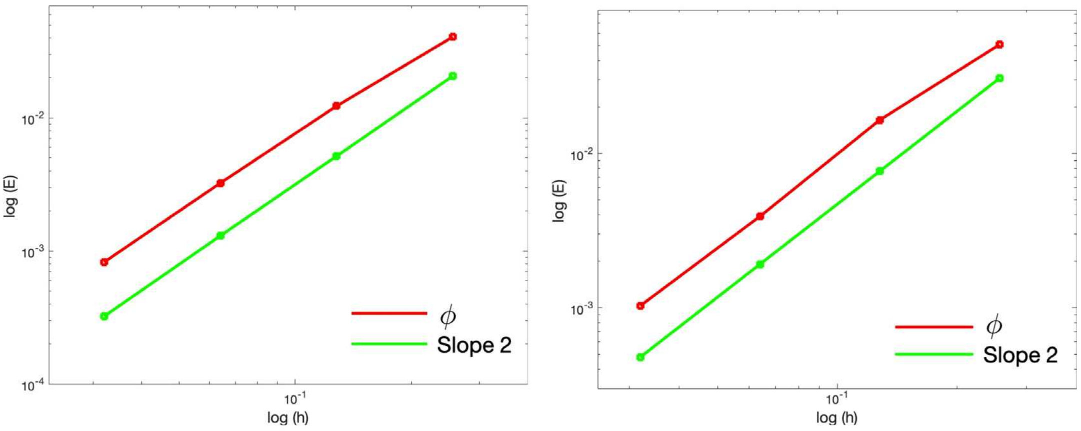

(a) Allen-Cahn.

(b) Cahn-Hilliard.

Fig. 4.1. (a) Convergence rate of our scheme for the Allen–Cahn system; and (b) Convergence rate of our scheme for the Cahn–Hilliard system.

We define the set of parameters $B = 1\text{e}4,\ \epsilon = 1\text{e}{-4},\ S = 4$, and the initial condition $\phi_0 = 0.1\cos(2x) + 0.2\cos(y)$. To obtain the convergence rate, a series of uniform meshes $\mathcal{S}_{h_i}$ from coarse to refined are performed, where the numbers of the vertex valence are in $[4, 6]$, and h_i is the mesh size. Since the subdivision-based IGA method is second-order accurate (cf. [26]), we set the time step sizes $\delta t_i = Ch_i$ for the ith level surface mesh $\mathcal{S}_{h_i}$ where C is a given constant between 0 and 1. Because the exact solution is unknown for us, we choose the solution obtained with a very fine mesh size computed as the benchmark solution which is treated approximately as the exact solution to compute the numerical errors. The L^2 numerical errors of two schemes are plotted in Fig. 4.1 when $t = 2.56\text{e}{-1}$, where the total numbers of patches/vertices for these surface models are 512/258, 2048/1026, 8192/4098, 32768/16386, and the corresponding mesh sizes $h_i = 0.2543,\ 0.1169,\ 0.0622,\ 0.0326$, respectively. We observe that both schemes possess the second-order accuracy for space.

4.2. Phase separation dynamics on curved complex surfaces

In this section, we carry out the phase separation (spinodal decomposition) simulations for both of the Allen–Cahn system and the Cahn–Hilliard system. The initial conditions are set as

$$\phi_0 = 0.001\text{rand}(x, y, z), \tag{4.2}$$

where the term rand(x, y, z) is the random number in $[-1, 1]$ with zero mean.

4.2.1. Allen–Cahn system

We first implement the scheme (3.45)–(3.49) for the Allen–Cahn system by setting the computation domain as a sphere, i.e., $\mathcal{S}_1 = \{(x, y, z) : \sqrt{x^2 + y^2 + z^2} = 10\}$. This surface is discretized with 32768 Loop limit subdivision patches by use of 16386 control vertices in Fig. 4.2, where the span of the vertex valence is 4 to 6. We set the model parameters $\delta t = 3\text{e}{-2}, B = 7\text{e}3, \epsilon = 3\text{e}{-2}$, and $S = 4$. We present the snapshots of the profile for the phase-field variable ϕ at the computational time steps of 10, 20, 40, 70, 100, 200, and 8000, where the phase separation dynamics evolve over time, and the final steady-state solution presents a two-layer pattern.

We further change the computational domain to an annular region, which is inside the domain $\mathcal{S}_2 = \{(x, y, z) : x \in [-4.98, 4.98],\ y \in [-4.98, 4.98],\ z \in [-1.32, 1.32]\}$. The surface is discretized with 51200 Loop limit subdivision patches by use of 25600 control vertices, and the span of the vertex valence is 4 to 6. The model parameters are taken as $\delta t = 1\text{e}{-2}, B = 8\text{e}3,\ \epsilon = 6\text{e}{-3}$, and $S = 4$. In Fig. 4.3, we plot the snapshots of the numerical solution ϕ at the computational time steps of 10, 20, 50, 100, 200, 280, and 6000. The final steady state solution also appears to be a two-layer mode, however, since the Allen–Cahn system is not volume-conserving, we can see that the blue region ($\phi = -1$) expands, the red region ($\phi = 1$) shrinks slightly.

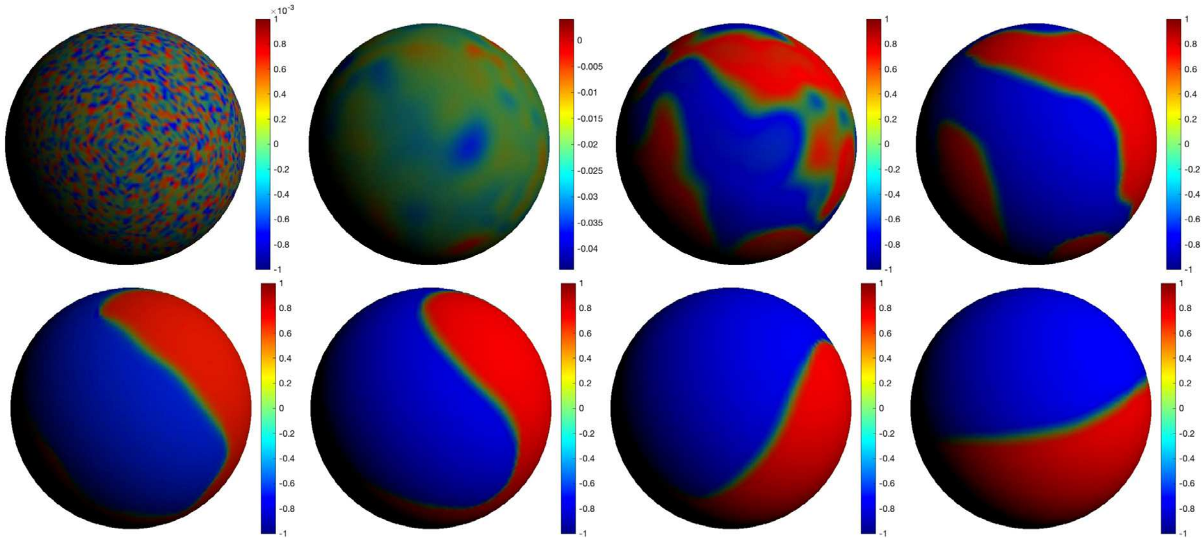

Fig. 4.2. The Allen–Cahn system for a closed sphere $\mathcal{S}_1$, where the first subfigure is the profile of the initial value ϕ_0, and all other subfigures correspond to the computation time steps of 10, 20, 40, 70, 100, 200 and 8000, respectively.

We continue to carry out simulation on a more complex "bunny" surface, which is within the domain $\mathcal{S}_3 = \{(x, y, z) : x \in [-9.12, 6.27],\ y \in [-3.38, 18.72],\ z \in [-6.49, 6.08]\}$. The surface is discretized with 144046 Loop subdivision patches by use of 72047 control points, and the span of the vertex valence is [3, 10]. We set the model parameters $\delta t = 4\text{e}{-3}$, $B = 9\text{e}3$, $\epsilon = 5\text{e}{-3}$, and $S = 4$. Snapshots of the profile for the phase-field variable ϕ are taken at the computational time steps of 20, 40, 60, 100, 200, 400 and 6000 in Fig. 4.4 respectively.

Finally, we verify the energy stability of the developed scheme. For the numerical test in Fig. 4.3, we choose three different time step sizes $\delta t = 1\text{e}{-2}$, $5\text{e}{-3}$ and $2.5\text{e}{-3}$ and plot the evolution of the energy curves in Fig. 4.5. The energy curves show the decays for the different time step sizes, which confirm our algorithm is unconditional energy stable.

4.2.2. Cahn–Hilliard system

To verify the effectiveness of the proposed scheme (3.54)–(3.58) for the Cahn–Hilliard equation, in this subsection, we carry out phase separation simulations on a number of complex surfaces. The first one is on the concave surface model within the domain $\mathcal{S}_4 = \{(x, y, z) : x \in [-3.08, 3.08],\ y \in [-3.08, 3.08],\ z \in [-0.69, 0.69]\}$, shown in Fig. 4.6. The surface is discretized with 32768 Loop subdivision patches by using 16386 control vertices, and the span of the vertex valence is 4 to 6. The model parameters are set as $\delta t = 2\text{e}{-3}$, $B = 1\text{e}4$, $\epsilon = 2\text{e}{-3}$, and $S = 4$. In Fig. 4.6, the snapshots of the phase-field variable ϕ are presented at the computational time steps of 20, 30, 100, 300, 500, 1500, and 8000, where the final equilibrium solution presents a striped pattern on the concave surface.

In Fig. 4.7, the phase separation simulation is carried out on a splayed surface model $\mathcal{S}_5 = \{(x, y, z) : x \in [-0.61, 0.61],\ y \in [-1.27,\ 1.27],\ z \in [-0.26,\ 0.26]\}$, which is discretized with 24576 Loop subdivision patches using 12286 control vertices, and the span of the vertex valence is 4 to 8. We choose the time step size $\delta t = 2\text{e}{-4}$ and the parameters $B = 1\text{e}4$, $\epsilon = 1.8\text{e}{-4}$, and $S = 4$. The snapshots of the phase-field variable ϕ are taken at the computation time steps of 30, 50, 100, 500, 1200, 2400, and 8000, where the steady state is achieved after around 3000 time steps.

We continue to carry out the phase separation simulation on a more complex human head surface model within the domain $\mathcal{S}_6 = \{(x, y, z) : x \in [-3.46, 3.46],\ y \in [-4.97,\ 4.97], z \in [-4.96,\ 4.96]$ in Fig. 4.8. The surface of the human head is discretized with 268686 Loop subdivision patches using 134,345 control vertices, and the span of the vertex valence is 3 to 12. We use the time step size $\delta t = 1\text{e}{-3}$ and the parameters $B = 1\text{e}4$, $\epsilon = 1.2\text{e}{-3}$, and $S = 4$. In Fig. 4.8, snapshots of the profiles for the phase-field variable ϕ are taken at the time steps of 30,

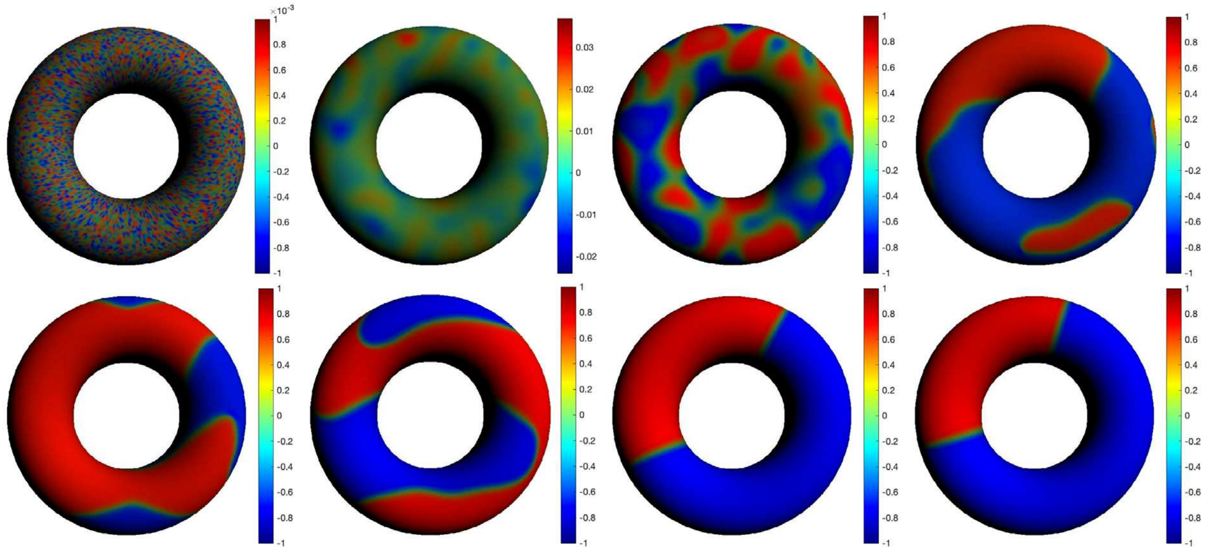

Fig. 4.3. The Allen–Cahn system for a ring $\mathcal{S}_2$, where the first subfigure is the profile of the initial value ϕ_0, and all other subfigures correspond to the computation time steps of 10, 20, 50, 100, 200, 280, and 6000, respectively.

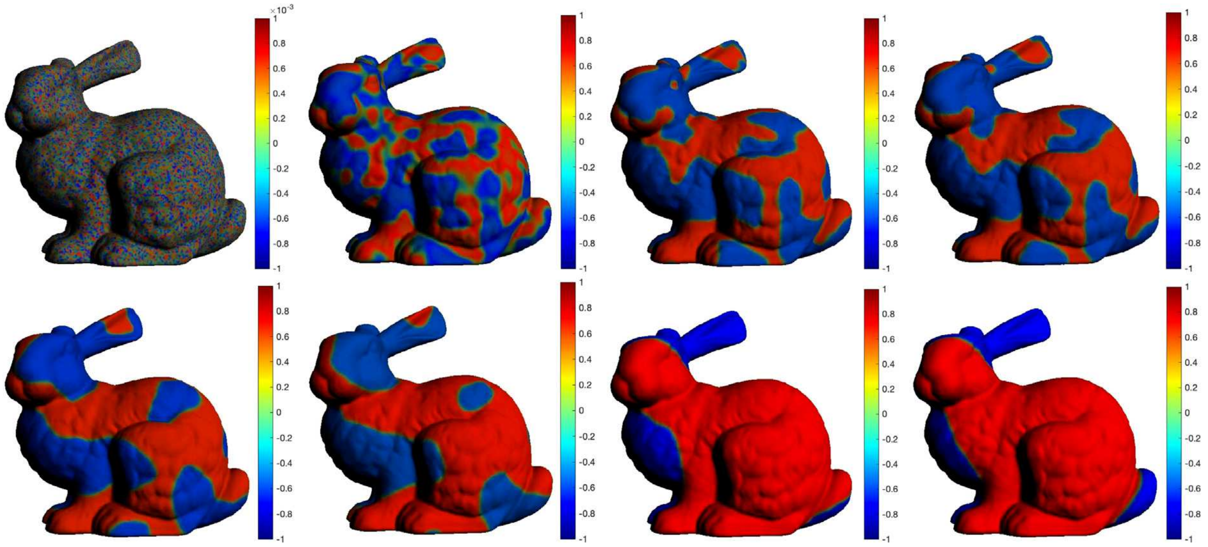

Fig. 4.4. The Allen–Cahn system for a bunny model $\mathcal{S}_3$, where the first subfigure is the profile of the initial value ϕ_0, and all other subfigures correspond to the computation time steps of 20, 40, 60, 100, 200, 400 and 6000, respectively.

100, 300, 500, 1000, 2000, and 8000, respectively, where the final equilibrium solution is observed after around 3000 time steps.

Finally, to show the energy stability, we choose three different time step sizes $\delta t = 2\text{e}{-3}, 1\text{e}{-3}$ and $5\text{e}{-4}$ to test the energy evolution of the numerical example given in Fig. 4.6. In Fig. 4.9, we plot the evolution of the energy curves that show the energy monotonically decays with respect to time. We can observe that the energy decrease decays very fast in the early stage of evolution, and tends to be flat in the later stage. The energy curves show the decays for the different time step sizes, which confirm our algorithm is unconditional energy stable.

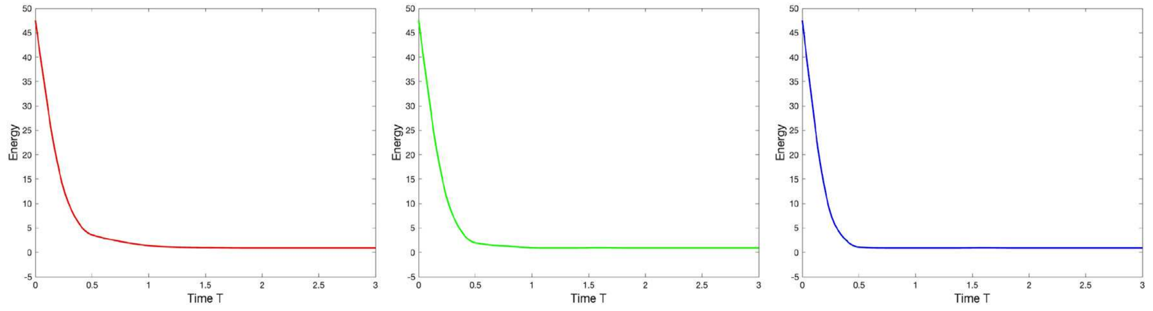

(a) (b) (c)

Fig. 4.5. The Allen–Cahn system for the ring in Fig. 4.3: Time evolution of the free energy for three different time step sizes δt = 1e−2, 5e−3 and 2.5e−3 which are shown in (a), (b) and (c) respectively. The energy curves show the decays for the different time step sizes, that confirm our algorithm is unconditionally stable.

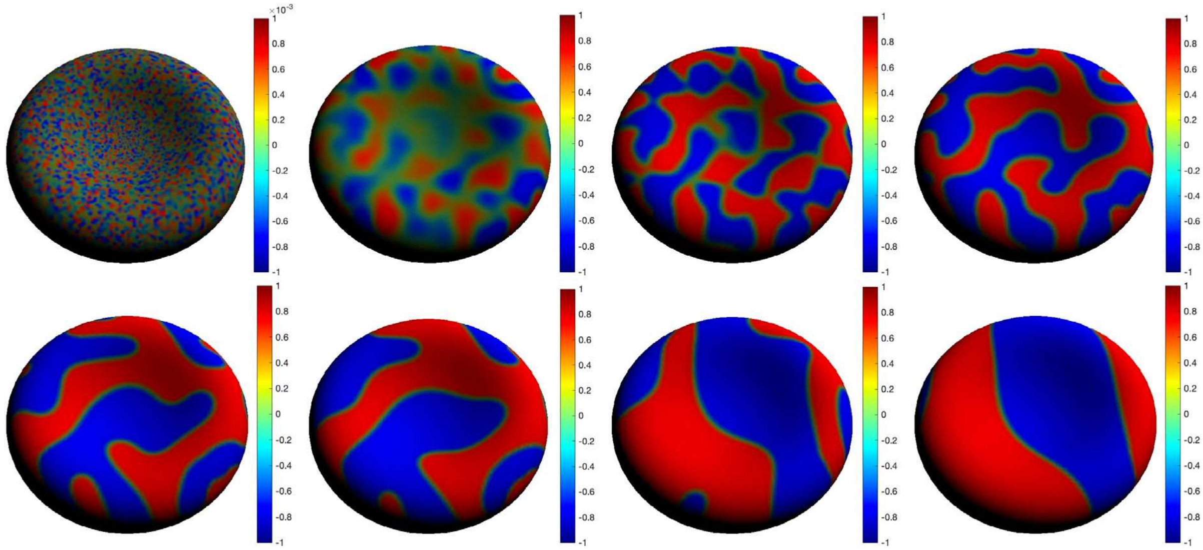

Fig. 4.6. The Cahn–Hilliard system for a concave surface $\mathcal{S}_4$, where the first subfigure is the profile of the initial value ϕ_0, and all other subfigures correspond to the computation time steps of 20, 30, 100, 300, 500, 1500 and 8000, respectively.

5. Conclusions

In this paper, we develop a fully discrete numerical strategy for solving the Allen–Cahn equation and the Cahn–Hilliard equation on complex curved surfaces. The scheme combines the subdivision-based IGA method for spatial discretization and the EIEQ method for time discretization. The advantages of the subdivision-based IGA method include the flexibility for complex surfaces with arbitrary topology structures and exactly expressible properties for geometries which can be remained unchanged throughout the h-refinement process. Its combination with the EIEQ method enables us to possess a linear, second-order accurate in time, decoupled, and unconditionally energy stable scheme. The high efficiency of the developed algorithm is shown by transforming the original highly nonlinear system into a few independent elliptic equations with only constant coefficients that only need to be solved at each time step. We also demonstrate unconditional energy stability and develop a decoupling-type implementation

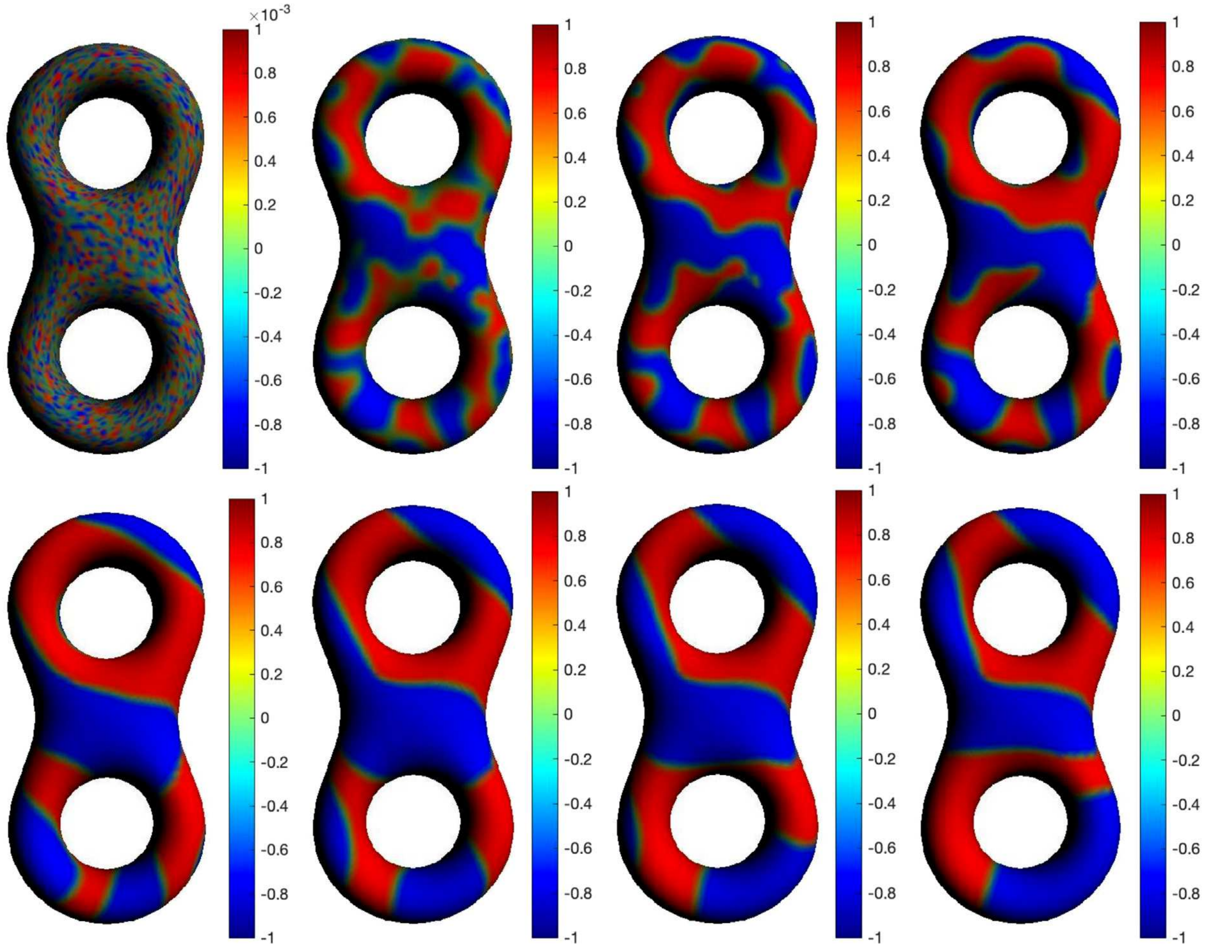

Fig. 4.7. The Cahn–Hilliard system for a splayed surface model $\mathcal{S}_5$, where the first subfigure is the profile of the initial value ϕ_0, and all other subfigures correspond to the computation time steps of 30, 50, 100, 500, 1200, 2400 and 8000, respectively.

strategy, and demonstrate the accuracy and stability of the developed numerical approach by simulating various numerical examples on the complex benchmark curved surfaces such as bunny, splayed, and head surfaces.

Declaration of competing interest

The authors declare that they have no known competing financial interests or personal relationships that could have appeared to influence the work reported in this paper.

Data availability

No data was used for the research described in the article.

Acknowledgments

The work of Q. Pan was partially supported by National Natural Science Foundation of China (No. 12171147 and 11971076). The work of C. Chen was partially funded by the key research project of Beijing Natural Science Foundation, China under Grant Z180002. The work of X. Yang was partially supported by National Science Foundation of USA with grant number DMS-2012490.

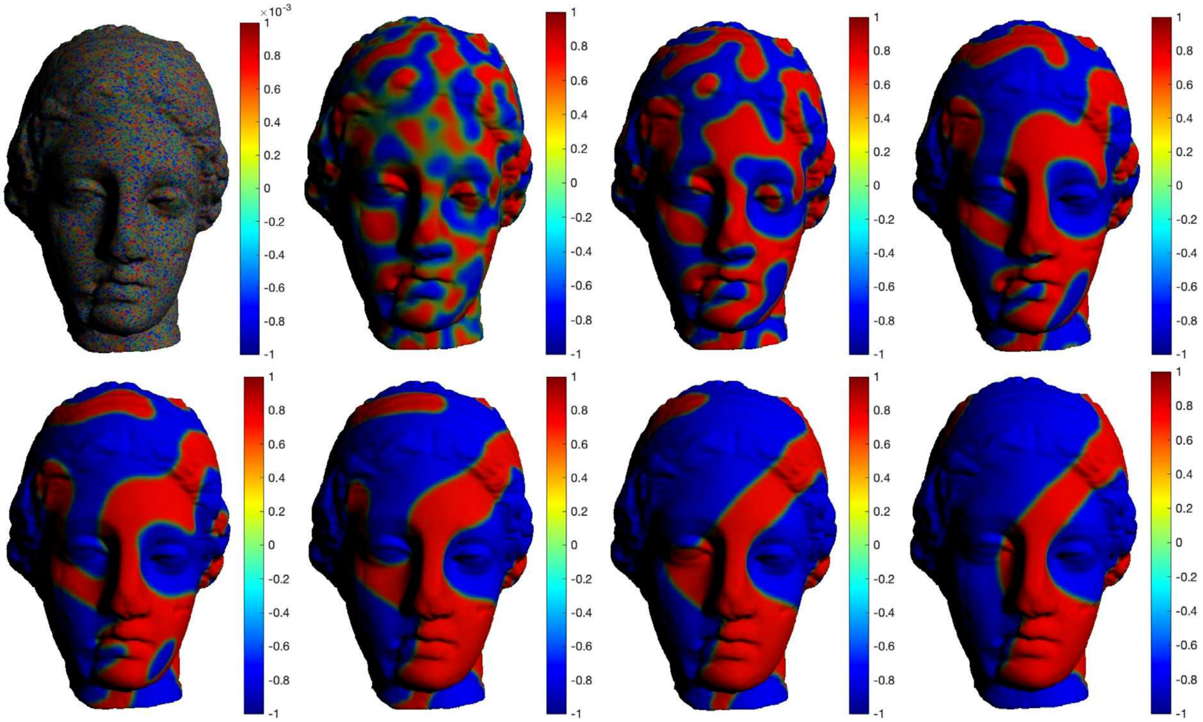

Fig. 4.8. The Cahn–Hilliard system for a head surface $\mathcal{S}_6$, where the first subfigure is the profile of the initial value ϕ_0, and all other subfigures correspond to the computation time steps of 30, 100, 300, 500, 1000, 2000 and 8000, respectively.

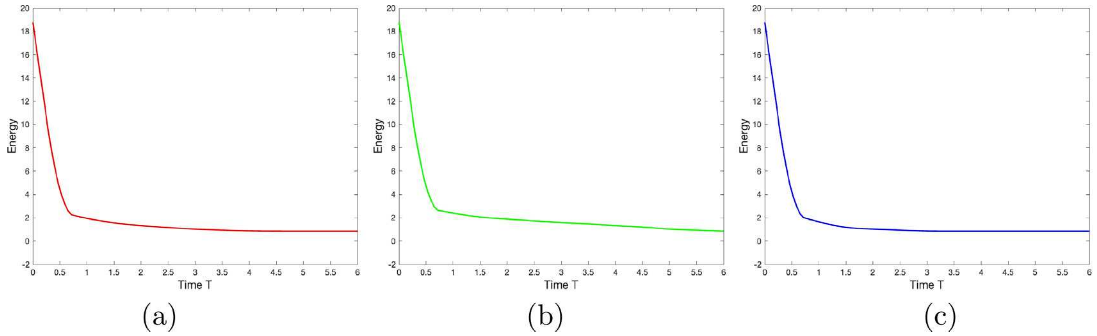

(a)

(b)

(c)

Fig. 4.9. The Cahn–Hilliard system for the concave surface model of Fig. 4.6: Time evolution of the free functional for three different time step sizes $\delta t = 2\mathrm{e}{-3}$, $1\mathrm{e}{-3}$ and $5\mathrm{e}{-4}$ which are shown in (a), (b) and (c) respectively. The energy curves show the decays for the different time step sizes, which confirm our algorithm is unconditionally stable.

References

[1] S.M. Allen, J.W. Cahn, A microscopic theory for antiphase boundary motion and its application to antiphase domain coarsening, Acta Metall. Mater. 27 (1979) 1085–1095.

[2] J.W. Cahn, J.E. Hilliard, Free energy of a nonuniform system. I. Interfacial free energy, J. Chem. Phys. 28 (2005) 258–267.

[3] F.A. Heberle, G.W. Feigenson, Phase separation in lipid membranes, Cold Spring Harb. Perspect. Biol. 3 (4) (2011) a004630.

[4] K. Yokota, T. Ogino, Phase separation in lipid bilayer membranes induced by intermixing at a boundary of two phases with different components, Chem. Phys. Lipids 191 (2015) 147–152.

[5] R. Parthasarathy, C. Yu, J.T. Groves, Curvature-modulated phase separation in lipid bilayer membranes, Langmuir 22 (11) (2006) 5095–5099.

[6] L. Ortellado, L.R. Góme, phase-field modeling of dendritic growth on spherical surfaces, Front. Mater. 7 (2020) 00163.

[7] D. Furihata, A stable and conservative finite difference scheme for the Cahn-Hilliard equation, Numer. Math. 87 (2001) 675–699.

[8] H.G. Lee, J.S. Lowengrub, J. Goodman, Modeling pinchoff and reconnection in a Hele-Shaw cell. II. Analysis and simulation in the nonlinear regime, Phys. Fluids 14 (2002) 514–545.

[9] C. Liu, J. Shen, A phase-field model for the mixture of two incompressible fluids and its approximation by a Fourier-spectral method, Physica D 179 (2003) 211–228.

[10] G. Dziuk, C.M. Elliot, Finite element methods for surface PDEs, Acta Numer. 22 (2013) 289–396.

[11] S. Zhao, X. Xiao, X. Feng, An efficient time adaptively based on chemical potential for surface Cahn-Hilliard equation using finite element approximation, Appl. Math. Comput. 369 (2020) 124901.

[12] Q. Du, L. Ju, L. Tian, Finite element approximation for the Cahn-Hilliard equation on surface, Comput. Methods Appl. Mech. Engrg. 200 (2011) 2458–2470.

[13] D. Marenduzzo, E. Orlandini, Phase separation dynamics on curved surfaces, Soft Matter 9 (2013) 1178–1187.

[14] T.J.R. Hughes, J.A. Cottrell, Y. Bazilevs, Isogeometric analysis: CAD, finite elements, NURBS, exact geometry, and mesh refinement, Comput. Methods Appl. Mech. Engrg. 194 (2005) 4135–4195.

[15] Y. Bazilevs, L. Beirão da Veiga, J.A. Cottrell, T.J.R. Hughes, G. Sangalli, Isogeometric analysis: approximation, stability and error estimates for h-refined meshes, Math. Models Methods Appl. Sci. 16 (7) (2006) 1031–1090.

[16] L.A. Piegl, W. Tiller, The NURBS Book, second ed., in: Monographs in Visual Communication, Spinger-Verlag, New York, 1997.

[17] T.W. Sederberg, G.T. Finnigan, X. Li, H. Lin, H. Ipson, Watertight trimmed NURBS, ACM Trans. Graph. 27 (3) (2008) 1–8.

[18] Y. Zhang, Y. Bazilevs, S. Goswami, C. Bajaj, T.J.R. Hughes, Patient-Specific vascular NURBS modeling for isogeometric analysis of blood flow, Comput. Methods Appl. Mech. Engrg. 196 (29–30) (2007) 2943–2959.

[19] T.W. Sederberg, J. Zheng, A. Bakenov, A. Nasri, T-splines and T-NURCCs, ACM Trans. Graph. 22 (3) (2003) 477–484.

[20] Y. Bazilevs, V.M. Calo, J.A. Cottrell, J.A. Evans, T.J.R. Hughes, S. Lipton, M.A. Scott, T.W. Sederberg, Isogeometric analysis using T-splines, Comput. Methods Appl. Mech. Engrg. 5–8 (2010) 229–263.

[21] E. Catmull, J. Clark, Recursively generated B-spline surfaces on arbitrary topological meshes, Comput. Aided Des. 10 (6) (1978) 350–355.

[22] C. Loop, Smooth Subdivision Surfaces Based on Triangles (Master's thesis), Department of Mathematices, University of Utah, 1978.

[23] A. Bartezzaghi L. Dedè, A. Quarteroni, Isogeometric Analysis of high order Partial Differential Equations on surfaces, Comput. Methods Appl. Mech. Engrg. 295 (2015) 446–469.

[24] Q. Pan, G. Xu, G. Xu, Y. Zhang, Isogeometric analysis based on extended Loop's subdivision, J. Comput. Phys. 299 (15) (2015) 731–746.

[25] Q. Pan, C. Chen, G. Xu, Isogeometric finite element approximation of minimal surfaces based on extended Loop subdivision, J. Comput. Phys. 343 (2017) 324–339.

[26] Q. Pan, T. Rabczuk, G. Xu, C. Chen, Isogeometric analysis for surface PDEs with extended Loop subdivision, J. Comput. Phys. 398 (2019) 108892.

[27] Q. Pan, T. Rabczuk, C. Chen, Subdivision based isogeometric analysis for geometric flows, Internat. J. Numer. Methods Engrg. 123 (2022) 610–633.

[28] Q. Pan, G. Xu, G. Xu, Y. Zhang, Isogeometric analysis based on extended Catmull–Clark subdivision, Comput. Math. Appl. 71 (2016) 105–119.

[29] Q. Pan, T. Rabczuk, G. Xu, C. Chen, Isogeometric analysis of minimal surfaces on the basis of extended Catmull–Clark subdivisions, Comput. Methods Appl. Mech. Engrg. 337 (2018) 128–149.

[30] Q. Pan, T. Rabczuk, X. Yang, Subdivision-based isogeometric analysis for second order partial differential equations on surfaces, Comput. Mech. 68 (2021) 1205–1221.

[31] X. Wei, Y. Zhang, T.J.R. Hughes, M.A. Scott, Truncated hierarchical Catmull–Clark subdivision with local refinement, Comput. Methods Appl. Mech. Engrg. 291 (2015) 1–20.

[32] X. Wei, X. Li, Y.J. Zhang, T.J.R. Hughes, Tuned hybrid Non-Uniform subdivision surfaces with optimal convergence rates, Internat. J. Numer. Methods Engrg. 122 (9) (2021) 2117–2144.

[33] F. Cirak, M. Ortiz, P. Schröder, Subdivision surfaces: a new paradigm for thin-shell finite-element analysis, Internat. J. Numer. Methods Engrg. 47 (2000) 2039–2072.

[34] F. Cirak, M.J. Scott, E.K. Antonsson, M. Ortiz, P. Schröder, Integrated modeling, finite-element analysis, and engineering design for thin-shell structures using subdivision, Comput. Aided Des. 34 (2) (2002) 137–148.

[35] X. Yang, Linear, first and second order and unconditionally energy stable numerical schemes for the phase-field model of homopolymer blends, J. Comput. Phys. 327 (2016) 294–316.

[36] M. Wang, Q. Huang, C. Wang, A Second Order Accurate Scalar Auxiliary Variable (SAV) Numerical Method for the Square Phase Field Crystal Equation, J. Sci. Comput. 88 (2021) 33.

[37] Q. Cheng, C. Wang, Error Estimate of a Second Order Accurate Scalar Auxiliary Variable (SAV) Numerical Method for the Epitaxial Thin Film Equation, Adv. Appl. Math. Mech. 6 (2021) 1318–1354.

[38] J. Guo, C. Wang, S. Wise, X. Yue, An H^2 convergence of a second-order convex-splitting, finite difference scheme for the three-dimensional Cahn–Hilliard equation, Commun. Math. Sci. 14 (2016) 489–515.

[39] X. Yang, On a novel fully-decoupled, linear and second-order accurate numerical scheme for the Cahn–Hilliard–Darcy system of two-phase Hele–Shaw flow, Comput. Phys. Comm. 263 (2021) 107868.

[40] X. Yang, A novel decoupled second-order time marching scheme for the two-phase incompressible Navier–Stokes/Darcy coupled nonlocal Allen–Cahn model, Comput. Methods Appl. Mech. Engrg. 377 (2021) 113597.

[41] J. Zhang, X. Yang, Efficient and accurate numerical scheme for a magnetic-coupled phase-field-crystal model for ferromagnetic solid materials, Comput. Methods Appl. Mech. Engrg. 371 (2020) 113310.

[42] X. Yang, Efficient and energy stable scheme for the hydrodynamically coupled three components Cahn-Hilliard phase-field model using the stabilized-Invariant Energy Quadratization (S-IEQ) Approach, J. Comput. Phys. 438 (2021) 110342.

[43] C. Chen, X. Yang, Efficient numerical schemes for a dendritic solidification phase-field model with melt convection, J. Comput. Phys. 388 (2019) 41–62.

[44] X. Yang, Linear, first and second-order, unconditionally energy stable numerical for the phase-field model of homopolymer blends, J. Comput. Phys. 327 (2016) 294–316.

[45] X. Yang, On a novel full decoupling, linear, second-order accurate, and unconditionally energy stable numerical scheme for the anisotropic phase-field dendritic crystal growth model, Internat. J. Numer. Methods Engrg. 122 (2021) 4129–4153.

[46] J. Stam, Fast evaluation of loop triangular subdivision surfaces at arbitrary parameter values, in: SIGGRAPH ’98, 1998, CD-ROM supplement.